The Silicon Vertex Detector of the Belle II Experiment

Y. Uematsu[q], K. Adamczyk[t], L. Aggarwal[i], H. Aihara[q], T. Aziz[j], S. Bacher[t], S. Bahinipati[f], G. Batignani[k,l], J. Baudot[e], P. K. Behera[g], S. Bettarini[k,l], T. Bilka[c], A. Bozek[t], F. Buchsteiner[b], G. Casarosa[k,l], L. Corona[k,l], T. Czank[p], S. B. Das[h], G. Dujany[e], F. Forti[k,l], M. Friedl[b], A. Gabrielli[m,n], E. Ganiev[m,n], B. Gobbo[n], S. Halder[j], K. Hara[r,o], S. Hazra[j], T. Higuchi[p], C. Irmler[b], A. Ishikawa[r,o], H. B. Jeon[s], Y. Jin[m,n], C. Joo[p], M. Kaleta[t], A. B. Kaliyar[j], J. Kandra[c], K. H. Kang[s], P. Kapusta[t], P. Kodyš[c], T. Kohriki[r], M. Kumar[h], R. Kumar[i], C. La Licata[p], K. Lalwani[h], S. C. Lee[s], J. Libby[g], S. N. Mayekar[j], G. B. Mohanty[j], T. Morii[p], K. R. Nakamura[r,o], Z. Natkaniec[t], Y. Onuki[q], W. Ostrowicz[t], A. Paladino[k,l], E. Paoloni[k,l], H. Park[s], G. Polat[d], K. K. Rao[j], I. Ripp-Baudot[e], G. Rizzo[k,l], D. Sahoo[j], C. Schwanda[b], J. Serrano[d], J. Suzuki[r], S. Tanaka[r,o], H. Tanigawa[q], R. Thalmeier[b], R. Tiwari[j], T. Tsuboyama[r,o], O. Verbycka[t], L. Vitale[m,n], K. Wan[q], Z. Wang[q], J. Webb[a], J. Wiechczynski[l], H. Yin[b], L. Zani[d],

(Belle-II SVD Collaboration)

[a] *School of Physics, University of Melbourne, Melbourne, Victoria 3010, Australia*
[b] *Institute of High Energy Physics, Austrian Academy of Sciences, 1050 Vienna, Austria*
[c] *Faculty of Mathematics and Physics, Charles University, 121 16 Prague, Czech Republic*
[d] *Aix Marseille Université , CNRS/IN2P3, CPPM, 13288 Marseille, France*
[e] *IPHC, UMR 7178, Université de Strasbourg, CNRS, 67037 Strasbourg, France*
[f] *Indian Institute of Technology Bhubaneswar, Satya Nagar, India*
[g] *Indian Institute of Technology Madras, Chennai 600036, India*
[h] *Malaviya National Institute of Technology Jaipur, Jaipur 302017, India*
[i] *Punjab Agricultural University, Ludhiana 141004, India*
[j] *Tata Institute of Fundamental Research, Mumbai 400005, India*
[k] *Dipartimento di Fisica, Università di Pisa, I-56127 Pisa, Italy*
[l] *INFN Sezione di Pisa, I-56127 Pisa, Italy*
[m] *Dipartimento di Fisica, Università di Trieste, I-34127 Trieste, Italy*
[n] *INFN Sezione di Trieste, I-34127 Trieste, Italy*
[o] *The Graduate University for Advanced Studies (SOKENDAI), Hayama 240-0193, Japan*
[p] *Kavli Institute for the Physics and Mathematics of the Universe (WPI), University of Tokyo, Kashiwa 277-8583, Japan*
[q] *Department of Physics, University of Tokyo, Tokyo 113-0033, Japan*
[r] *High Energy Accelerator Research Organization (KEK), Tsukuba 305-0801, Japan*
[s] *Department of Physics, Kyungpook National University, Daegu 41566, Korea*
[t] *H. Niewodniczanski Institute of Nuclear Physics, Krakow 31-342, Poland*

Abstract

The Silicon Vertex Detector (SVD) is a part of the vertex detector in the Belle II experiment at the SuperKEKB collider (KEK, Japan). Since the start of data taking in spring 2019, the SVD has been operating stably and reliably

Email address: uematsu@hep.phys.s.u-tokyo.ac.jp (Y. Uematsu)

Preprint submitted to Nuclear Instruments and Methods A *November 13, 2021*

with a high signal-to-noise ratio and hit efficiency, achieving good spatial resolution and high track reconstruction efficiency. The hit occupancy, which mostly comes from the beam-related background, is currently about 0.5% in the innermost layer, causing no impact on the SVD performance. In anticipation of the operation at higher luminosity in the next years, two strategies to sustain the tracking performance in future high beam background conditions have been developed and tested on data. One is to reduce the number of signal waveform samples to decrease dead time, data size, and occupancy. The other is to utilize the good hit-time resolution to reject the beam background hits. We also measured the radiation effects on the sensor current, strip noise, and full depletion voltage caused during the first two and a half years of operation. The results show no detrimental effect on the SVD performance.

Keywords: Silicon strip detector, Vertex detector, Tracking detector, Belle II

1. Introduction

The Belle II experiment [1] aims to probe new physics beyond the Standard Model in high-luminosity e^+e^- collision at the SuperKEKB collider (KEK, Japan) [2]. The SuperKEKB consists of injector LINAC, positron dumping ring, and main storage ring with the electron and positron beamlines. The Belle II detector is located at the interaction point (IP) of the two beamlines. The main collision energy in the center-of-mass system is 10.58 GeV on the $\Upsilon(4S)$ mass-resonance, which enables various physics programs based on the high statistics of B-mesons, τ-leptons, and D-mesons. Also, the asymmetric energy of the 7-GeV electron beam and 4-GeV positron beam is adopted for the time-dependent CP violation measurement. The target of SuperKEKB is to accumulate integrated luminosity of 50 ab^{-1} with peak luminosity of about 6×10^{35} $cm^{-2}s^{-1}$. In June 2021, SuperKEKB recorded the wolrd's highest instantaneous luminosity of 3.1×10^{34} $cm^{-2}s^{-1}$. The data accumulated before July 2021 is 213 fb^{-1}.

The Vertex Detector (VXD) is the innermost detector in the Belle II detector system. The VXD has six layers: the inner two layers (layers-1 and 2) are the

Pixel Detector (PXD), and the outer four layers (layers-3 to 6) are the Silicon Vertex Detector (SVD). The schematic cross-sectional view of the VXD is shown in Fig. 1. The PXD consists of DEPFET pixel sensors, and its innermost radius is 1.4 cm from the IP. Detailed descriptions of the SVD appear in Sec. 2.

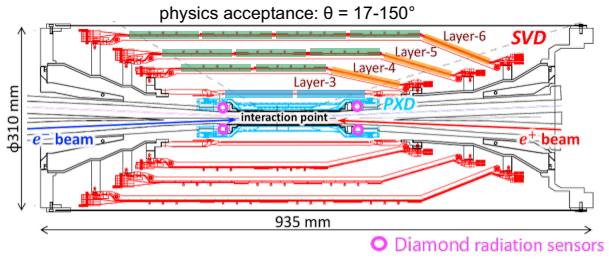

Figure 1: Schematic cross-sectional view of the VXD. The SVD is in red, the PXD in light-blue, and the IP beam pipe diamonds in pink circles. The locations of the three types of DSSDs are indicated by boxes in three colors: blue for small sensors, green for large sensors, and orange for trapezoidal sensors as described in Tab. 1.

Besides the VXD, diamond sensors [3] are mounted on the IP beam pipe and the bellows pipes outside of the VXD. The pink circles in Fig. 1 indicate the locations of the diamond sensors on the IP beam pipe. They measure the dose rates in these locations. The measured doses are used to estimate the dose in the SVD. They also send beam abort requests to SuperKEKB if the radiation level gets too high to avoid severe damage to the detector.

2. Belle II Silicon Vertex Detector

The SVD is crucial for extrapolating the tracks to the PXD. This task is essential for measuring the decay vertices with the PXD and pointing at a region-of-interest limiting the PXD readout volume. Also, the SVD plays a critical role in the decay vertex measurement in case long-lived particles like K_S decay inside the SVD volume. Other roles of the SVD are the standalone track reconstruction of low-momentum charged particles and their particle identification using energy deposit $\mathrm{d}E/\mathrm{d}x$.

The SVD [4] consists of four layers of Double-sided Silicon Strip Detectors (DSSDs). The material budget of the SVD is about 0.7% X_0 per layer. The readout Aluminum strips are AC-coupled to every other n/p-side strips (electrodes) on the n-type substrate over the silicon oxide layer. On each DSSD plane, a local coordinate is defined with u and v: u-axis along n-side strips and v-axis perpendicular to u-axis. In other words, p-side strips and n-side strips provide u and v information, respectively. In the cylindrical coordinate, u corresponds to r–φ information and v corresponds to z information. The SVD consists of three types of sensors: "small" sensors in layer-3, "large" sensors in layer-456 barrel region, and "trapezoidal" sensors in layer-456 forward/slanted region. They are indicated in blue, green, and orange boxes in Fig. 1. The dimensions for these three types of sensors are summarized in Tab. 1. The sensors are manufactured by two companies: the small and large sensors by Hamamatsu and trapezoidal sensors by Micron. The full depletion voltage is 60 V for Hamamatsu sensors, 20 V for Micron sensors, and both types of sensors are operated at 100 V. In total, 172 sensors are assembled, corresponding to a total sensor area of 1.2 m^2 and 224,000 readout strips.

	Small	Large	Trapezoidal
No. of u/p-strips	768	768	768
u/p-strip pitch	50 μm	75 μm	50–75 μm
No. of v/n-strips	768	512	512
v/n-strip pitch	160 μm	240 μm	240 μm
Thickness	320 μm	300 μm	300 μm
Manufacturer	Hamamatsu		Micron

Table 1: Table of dimensions for three types of sensors. Only readout strips are taking into account for number of strips and strip pitch.

The front-end ASIC used in the SVD is APV25 [5], which was originally developed for CMS silicon tracker. APV25 is radiation hard for over 100 Mrad radiation. It has 128 channel inputs and shapers for each channel with a shaping

time of about 50 ns. For the SVD, APV25 is operated in "multi-peak" mode. The mechanism of the data sampling in the multi-peak mode is explained in Fig. 2. The chip samples the height of the signal waveform with the 32 MHz clock and stores each sampled information in the analog ring buffer. Since the bunch-crossing frequency is eight times faster than the sampling clock, the stored samples are not synchronous to the beam collision in contrast to CMS, which motivates to operate in the multi-peak mode. In the present readout configuration (the six-samples mode), at every reception of the Belle II global Level-1 trigger, the chip reads out successive six samples of the signal waveform stored in the buffers. The six-samples mode offers enough time window ($6 \div 32\,\mathrm{MHz} = 187\,\mathrm{ns}$) which accepts large timing shifts of the trigger. In preparation for operation with higher luminosity, where background occupancy, trigger dead-time, and the data size increase, we developed the three/six-mixed acquisition mode (mixed-mode). The mixed-mode is a new method to read out the signal samples from APV25, in which the number of the samples changes between three and six in each event, depending on the timing precision of each Level-1 trigger signal in that event. For triggers with good timing precision, three-samples data are read out and the data have half time window and half data size compared to ones of six-samples data, resulting in the reduction of the effect due to higher luminosity. This functionality was already implemented in the running system and confirmed by a few hours of smooth physics data-taking. Before we start to use the mixed-mode, the effect on the performance due to the change of the acquisition mode is to be assessed. As the first step, the effect in the hit efficiency was evaluated as described in Sec. 3.

The APV25 chips are mounted on each middle sensor (chip-on-sensor concept) with thermal isolation foam in between. The merit of this concept is shorter signal propagation length, leading to the smaller capacitance of the signal line and hence the smaller noise level. To reduce the material budget the APV25 chips on the sensor are thinned down to 100 μm. APV25s are mounted on the single side of the sensor and read out the signals from the other side via wrapped flexible printed circuits. The power consumption of the APV25 chip

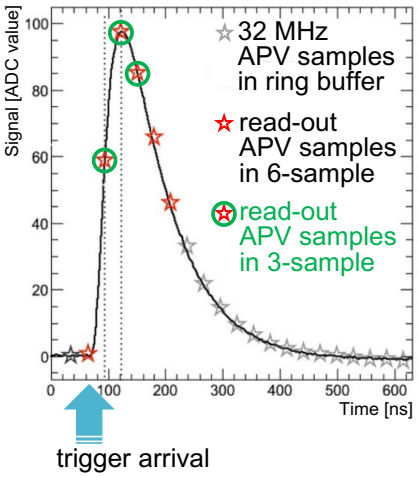

Figure 2: The plot explains the sampling in the "multi-peak" mode of APV25. The black line shows the signal waveform after the CR-RC shaper circuit. The stars show the sampled signal height recorded in the analog ring buffer according to the 32 MHz sampling clock. The red stars indicate the six successive samples read out at the trigger reception in the six-samples mode. The red stars with a green circle indicate the samples read out in the three-samples acquisition.

is 0.4 W/chip and in total 700W in the entire SVD. The chips are chilled by bi-phase –20°C CO_2.

3. Performance

The SVD was combined with the PXD to complete the VXD assembly in October 2018, and the VXD was installed to the Belle II detector system in November 2018. Since March 2019, the SVD has been operating reliably and smoothly for two and a half years, without any major problems. The total fraction of masked strips is about 1%. There was only one issue where one APV25 chip (out of 1,748 chips) was disabled during the spring of 2019, which was gone after cable reconnection in the summer of 2019.

The SVD has also demonstrated stable and excellent performance [6]. The hit efficiency is stably over 99% in most of the sensors. The cluster charge dis-

tributions are also reasonable. On the u/p-side, the most probable values agree with the calculated charge amount induced by MIPs within the uncertainty in calibration. On the v/n-side, 10–30% of the collected charge losses compared to MIP due to the smaller inter-strip capacitance of the floating strips with larger strip pitches than the u/p-side. The most probable values of the cluster SNR distributions range from 13 to 30.

We measured the cluster position resolution by analyzing the $e^+e^- \to \mu^+\mu^-$ data [7]. The cluster position resolution is estimated from the residual between the cluster position and the track position not biased by the target cluster after subtracting the effect of the track extrapolation error. The cluster position resolutions for different incident angles are shown in Fig. 3. For normal incident tracks, it well agrees with the expectations from the strip pitch including floating strips. For tracks with an incident angle, it is expected to get a better resolution, which is indeed the case in the v/n-side results. However, this effect is not observed on the u/p-side, and the study is still ongoing to improve the cluster position estimation.

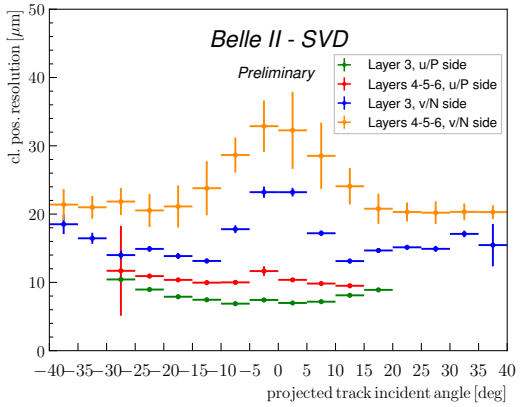

Figure 3: The SVD cluster position resolution depending on the projected track incident angle. The green(blue) plot shows the resolution in the u/p(n/v)-side of Layer 3 sensors, and the red(yellow) one shows the u/p(n/v)-side of Layers 4–6 sensors.

The cluster hit-time resolution was also evaluated using the reference event time estimated by the Central Drift Chamber (CDC) outside of SVD. The error

on the event time, about 0.7 ns, was subtracted to evaluate the intrinsic SVD hit-time resolution. The resulting resolution is 2.9 ns on the u/p-side and 2.4 ns on the v/n-side. With such precise hit-time information, it is possible to reject off-time background hits efficiently. The hit-time distributions for signal and off-time background are shown in Fig. 4. The signal distribution has a narrow peak, while the background hit-time distribution is broad and almost flat in the signal peak region. The separation power of the hit-time is high, as expected. For example, if we reject hits with the hit-time less than -38 ns in this plot, we can reject 46% of the background hits while keeping 99% of the signal hits. The background rejection based on the hit-time is essential to sustain the good tracking performance in the future high beam background condition.

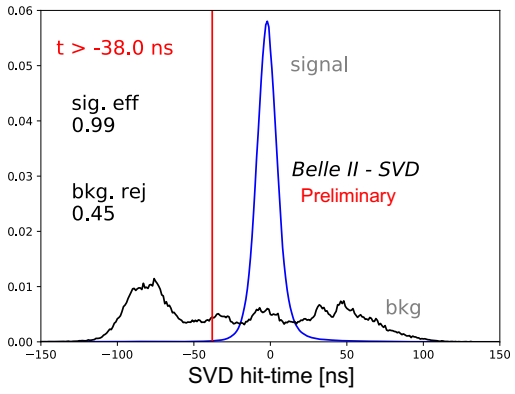

Figure 4: The plot shows an example of the background hit rejection using hit-time. The blue distribution shows the signal, and the black distribution shows the off-time background. Assuming the hit-time cut at -38 ns, the signal hit efficiency of 99% and the background hit rejection of 46% are achieved.

The performance in three-samples data was compared with that in six-samples data to evaluate the performance in the mixed-mode. If the trigger timing has no deviation, the three-samples data will show comparable performance to the six-samples data because the relevant part of the signal waveform to evaluate the necessary signal properties, which are the signal height and the signal timing, can be accommodated in the three-samples time window. How-

ever, when the trigger has a jitter and the timing shift happens, some part of the signal waveform can be out of the three-samples time window, and the reconstruction performance deteriorates. We examined the effect on the hit efficiency as a function of the trigger timing shift. The effect is evaluated by the relative hit efficiency, which is defined as the ratio of the hit efficiency in the three-samples data to the one in the six-samples data. For this study, the three-samples data are emulated in the offline analysis from the six-samples data by selecting consecutive three samples at fixed positions in the six samples. The trigger timing shift is evaluated by the CDC event time. The resulting relative efficiencies as a function of the trigger timing shift are shown in Fig. 5. The decreasing trend is observed for the shift of the trigger timing, as expected. As a result, the relative efficiency is over 99.9% for the trigger timing shift within $\pm$30 ns.

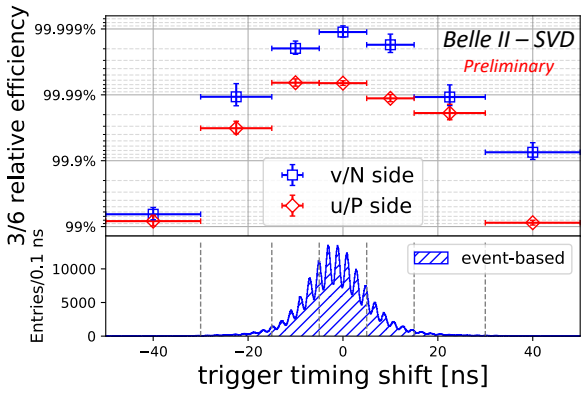

Figure 5: The relative hit efficiencies as a function of the trigger timing shift for v/n-side (blue square) and u/p-side(red diamond). The positive(negative) trigger timing shift corresponds to early(late) trigger timing.

4. Beam-related background effects on SVD

The beam-related background increases the hit occupancy of the SVD, which in turn degrades the tracking performance. Considering this performance degradation, we set the occupancy limit in layer-3 sensors to be about 3%, which will

be loosened roughly by a factor of two after we apply the hit-time rejection described in Sec. 3. With the current luminosity, the average hit occupancy in layer-3 sensors is less than 0.5%. However, the projection of the hit occupancy at the luminosity of 8×10^{35} $\mathrm{cm}^{-2}\mathrm{s}^{-1}$ is about 3% in layer-3 sensors. The projected occupancy comes from the Monte Carlo (MC) simulation scaled by the data/MC ratio determined from the beam background data of the current beam optics. The corresponding dose is about 0.2 Mrad/smy, and the equivalent 1-MeV neutron fluence is about 5×10^{11} $\mathrm{n_{eq}/cm^2/smy}$ (smy: Snowmass Year = 10^7 sec). The long-term extrapolation of the beam background is affected by large uncertainties from the optimization of collimator settings in MC and the future evolution of the beam injection background, which is not simulated. This uncertainty motivates the VXD upgrade which improves the tolerance of the hit rates and the radiation damages, and the technology assessment is ongoing for multiple sensor options.

From the measured dose on diamond sensors, the integrated radiation dose in the layer-3 mid-plane sensors, which are the most exposed in the SVD, is estimated to be 70 krad. The estimation is based on the correlation between the SVD occupancy and the diamonds dose. The estimated dose includes uncertainties of about 30% due to the unavailability of the appropriate trigger before December 2020. Assuming the dose/$\mathrm{n_{eq}}$ fluence ratio of 2.3×10^9 $\mathrm{n_{eq}/cm^2/krad}$ from MC, 1-MeV equivalent neutron fluence is evaluated to be about 1.6×10^{11} $\mathrm{n_{eq}/cm^2}$ in the first two and a half years.

The effect of the integrated dose on the sensor leakage current is measured, and the results show a clear linear correlation as in the upper plot of Fig. 6. The slopes for all the sensors are summarized in the lower plot of Fig. 6. They are around 2–5 $\mu\mathrm{A/cm^2/Mrad}$. The large variations can be explained by temperature effects and the deviation of sensor-by-sensor dose from the average in each layer used in the estimation. The slopes are in the same order of magnitude as previously measured in the BaBar experiment [8], 1 $\mu\mathrm{A/cm^2/Mrad}$ at 20°C. While the leakage current is increasing, the impact on the strip noise is suppressed by the short shaping time (50 ns) in APV25. It is expected to be

comparable to the strip-capacitive noise only after 10 Mrad irradiation and not problematic for ten years where the integrated dose is estimated to be 2 Mrad.

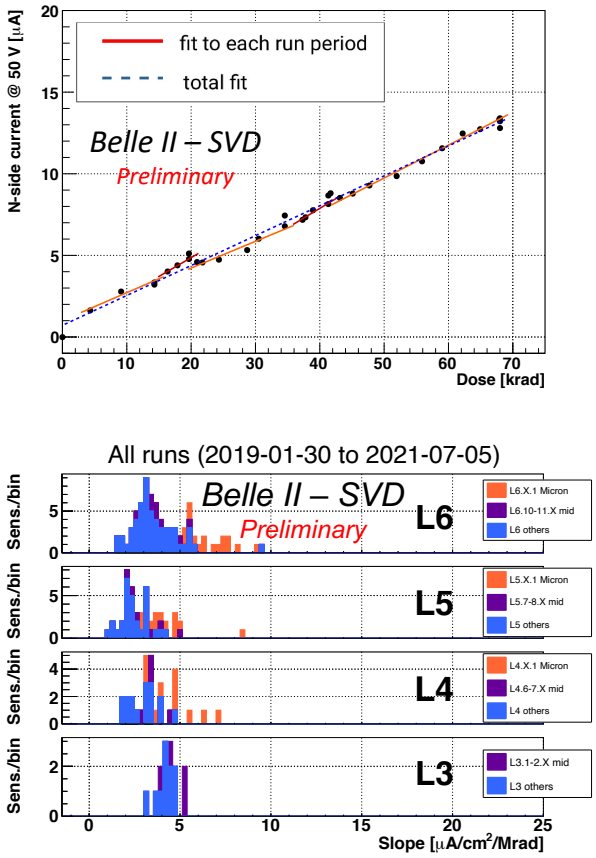

Figure 6: (upper) The effect of the integrated dose on the leakage current in the n/v-side of one layer-3 sensor. The slope is fitted for each run period (solid red line) and for all the runs (dashed blue line). Both fit results agree well with each other and are consistent with the linear increase. (lower) The fit results of all the sensors for all runs. The sensors are classified as trapezoidal sensors in the forward region, sensors around the midplane, and the others.

The relation between the noise and the integrated dose is shown in Fig. 7. The noise increase of 20–25% is observed in layer-3, but this does not affect the performance of SVD. This noise increase is likely due to the radiation effects on the sensor surface. Fixed oxide charges on sensor surface increase non-linearly, enlarging inter-strip capacitance. The noise saturation is observed on the v/n-

side and also starts to be seen on the u/p-side. This behavior agrees with the increase of fixed oxide charges.

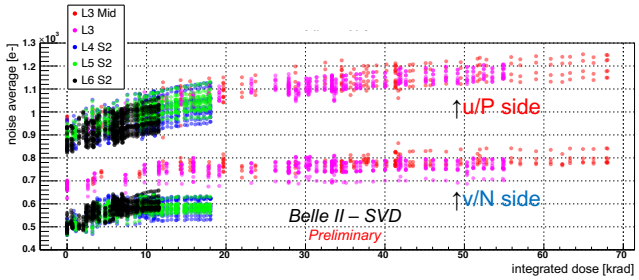

Figure 7: The effect of the integrated dose on the noise average in electron The clear increase is observed and saturated (or start to be saturated) for layer-3 sensors.

The full depletion voltage of the sensor is also a key property that can be affected by the radiation damage. It can be measured from the v/n-side strip noise, which suddenly decreases at the full depletion voltage because the sensor substrate is n-type and thus the v/n-side strips can be fully isolated at the full depletion. From this measurement, reasonable full depletion voltages, which are consistent with the values mentioned in Sec. 2, were confirmed, and so far no change in full depletion voltage is observed in the first two and a half years of operation, which is consistent with the expectation from low integrated neutron fluence of 1.6×10^{11} n_{eq}/cm^2.

5. Conclusions

SVD has been taking data in Belle II since March 2019 smoothly and reliably. The detector performance is excellent and agrees with expectations. We are ready to cope with the increased background in higher luminosity by rejecting the off-time background hits using hit-time and operating in the three/six-mixed acquisition mode. In the recent study, the efficiency loss in the three-samples data is confirmed to be less than 0.1% for the trigger timing shift within ±30ns. The observed first effects of radiation damage are also within expectation and do not affect the detector performance.

Acknowledgments

This project has received funding from the European Union's Horizon 2020 research and innovation programme under the Marie Sklodowska-Curie grant agreements No 644294 and 822070. This work is supported by MEXT, WPI, and JSPS (Japan); ARC (Australia); BMWFW (Austria); MSMT (Czechia); CNRS/IN2P3 (France); AIDA-2020 (Germany); DAE and DST (India); INFN (Italy); NRF-2016K1A3A7A09005605 and RSRI (Korea); and MNiSW (Poland).

References

[1] T. Abe, et al., Belle II Technical Design Report (2010). arXiv:1011.0352.

[2] Y. Ohnishi, et al., Accelerator design at SuperKEKB, Progress of Theoretical and Experimental Physics 2013 (3), 03A011 (03 2013).

[3] S. Bacher, et al., Performance of the diamond-based beam-loss monitor system of Belle II, Nucl. Instrum. Meth. A 997 (2021) 165157. arXiv:2102.04800.

[4] K. Adamczyk, et al., The belle ii silicon vertex detector assembly and mechanics, Nuclear Instruments and Methods in Physics Research Section A: Accelerators, Spectrometers, Detectors and Associated Equipment 845 (2017) 38–42, proceedings of the Vienna Conference on Instrumentation 2016.

[5] M. J. French, et al., Design and results from the APV25, a deep sub-micron CMOS front-end chip for the CMS tracker, Nuclear Instruments and Methods in Physics Research Section A: Accelerators, Spectrometers, Detectors and Associated Equipment 466 (2001) 359–365.

[6] G. Rizzo, et al., The Belle II Silicon Vertex Detector: Performance and Operational Experience in the First Year of Data Taking. arXiv:https://journals.jps.jp/doi/pdf/10.7566/JPSCP.34.010003.

[7] R. L. Boucher, et al., Measurement of the cluster position resolution of the Belle II Silicon Vertex Detector, these NIMA Conference Proceedings.

[8] B. Aubert, et al., The babar detector: Upgrades, operation and performance, Nuclear Instruments and Methods in Physics Research Section A: Accelerators, Spectrometers, Detectors and Associated Equipment 729 (2013) 615–701.